Department of Electrical and Computer
Engineering Faculty Publications

Department of Electrical and Computer
Engineering

2007

Ballistic graphene nanoribbon metal-oxide-semiconductor field-effect transistors: A full real-space quantum transport simulation

Gengchiau Liang
Harvard University

Neophytos Neophytou
Network for Computational Nanotechnology, Purdue University

Mark S. Lundstrom
Purdue University, lundstro@purdue.edu

Dmitri Nikonov
Intel Corporation

Ballistic graphene nanoribbon metal-oxide-semiconductor field-effect transistors: A full real-space quantum transport simulation

Gengchiau Liang[a)]
Electrical and Computer Engineering, National University of Singapore, Singapore 117576

Neophytos Neophytou and Mark S. Lundstrom
School of Electrical and Computer Engineering, Purdue University, West Lafayette, Indiana 47907-1285, USA

Dmitri E. Nikonov
Technology and Manufacturing Group, Intel Corp., SC1-05, Santa Clara, California 95052, USA

A real-space quantum transport simulator for graphene nanoribbon (GNR) metal-oxide-semiconductor field-effect transistors (MOSFETs) has been developed and used to examine the ballistic performance of GNR MOSFETs. This study focuses on the impact of quantum effects on these devices and on the effect of different type of contacts. We found that two-dimensional (2D) semi-infinite graphene contacts produce metal-induced-gap states (MIGS) in the GNR channel. These states enhance quantum tunneling, particularly in short channel devices, they cause Fermi level pinning and degrade the device performance in both the ON-state and OFF-state. Devices with infinitely long contacts having the same width as the channel do not indicate MIGS. Even without MIGS quantum tunneling effects such as band-to-band tunneling still play an important role in the device characteristics and dominate the OFF-state current. This is accurately captured in our nonequilibrium Greens' function quantum simulations. We show that both narrow (1.4 nm width) and wider (1.8 nm width) GNRs with 12.5 nm channel length have the potential to outperform ultrascaled Si devices in terms of drive current capabilities and electrostatic control. Although their subthreshold swings under forward bias are better than in Si transistors, tunneling currents are important and prevent the achievement of the theoretical limit of 60 mV/dec. © *2007 American Institute of Physics*. [DOI: 10.1063/1.2775917]

I. INTRODUCTION

Graphite-related materials such as fullerenes, graphene, and carbon nanotubes have generated considerable interest due to their unique electronic and optoelectronic properties. It has been demonstrated that carbon nanotubes (CNTs) exhibit quasiballistic conduction and can operate as transistors,[1] light emitters,[2,3] and sensors.[4] Similarly, two-dimensional (2D) graphene (i.e., a monolayer of graphite) sheets have been shown to possess very high carrier mobility. Unlike CNTs, the metallic nature of this material with zero band gap limits the use of 2D graphene sheets as semiconductor devices. Recently, graphene sheets have been patterned into narrow nanoribbons.[5,6] Due to quantum confinement, graphene nanoribbons (GNRs) acquire a band gap, which depends on their width and orientation relative to the graphene crystal structure.[7,8] Similar to CNTs, both semiconducting and metallic properties can be achieved by armchair graphene nanoribbons (GNRs) and zigzag GNRs,[7,8] respectively. Field-effect tannsistor (FET) type devices based on armchair GNRs have been studied both experimentally[9] and theoretically.[8,10,11] Recent studies using a semiclassical transport model predicted that GNR metal-oxide-semiconductor field-effect transistors (MOSFETs) might outperform traditional Si MOSFETs (Ref. 8) and could have a competitive

ON-current performance compared with CNT MOSFETs.[11] However, little is known about the role of quantum effects in GNR MOSFET device performance.[12] In particular, quantum effects such as tunneling, can play an important role by reducing the ratio of I_{ON} to I_{OFF}, and increase the subthreshold slope, thus degrade the device performance.

In this article, we present a full real-space quantum transport simulator based on the nonequilibrium Green's function (NEGF) approach, self-consistently coupled to a three-dimensional (3D) Poisson's solver for the treatment of electrostatics. We study the effect of the contacts on armchair GNR devices by considering both "one-dimensional (1D)" contacts (of width equal to that of the channel), and "2D" semi-infinite contacts. (By 1D, we mean infinitely long contacts having the same width as the channel. By 2D, we mean an infinitely long contact that is much wider than the channel.) We found that in the case of 2D contacts, metal-induced gap states (MIGS) form, and produce localized states in the middle of the band gap. These levels pin the Fermi level and contribute to tunneling when the channel is short, therefore degrading the device performance. Armchair GNR MOSFETs with 1D contacts display a clear band gap with no MIGS and are the main focus of this study.

We consider two GNR channels, a narrow one of 1.4 nm width and a wider one of 1.8 nm width. The channel length of the devices considered is 12.5 nm. The subthreshold slope (SS) of these two GNR MOSFETs is around 65 mV/decade

---

a)Electronic mail: elelg@nus.edu.sg

and 70 mV/decade respectively. The drain-induced-barrier-lowering (DIBL) is 30 mV/V and 53 mV/V respectively, which is smaller than the theoretically expected value of a double gate 10 nm scale Si MOSFET.[13] The reason for this performance enhancement in the GNR MOSFET case can be attributed to the nature of the GNR device, which consists of a single monolayer of carbon atoms (an ultimate ultrathin body, double gate MOSFET). The electrostatic control of such a device can be superior to other planar transistors, since it eliminates any degrading 2D electrostatic effects associated with the finite body thickness. The subthreshold slope of 60 mV/decade (fundamental thermal limit at room temperature), however, cannot be achieved in this operation mode. The light effective mass of GNRs, in combination with their small band gap and the short channel length, enhance carrier tunneling through the barrier from the source to the drain. This effect degrades the OFF-state device performance. On the other hand, this tunneling process can be utilized in other operating schemes, such as in band-to-band-tunneling (BTBT) devices. The subthreshold slope of the band-to-band-tunneling CNT MOSFET has been demonstrated to be smaller than the fundamental thermal limit.[14,15] Based on our simulations, the GNR MOSFETs may also be candidates for BTBT device applications.

II. APPROACH

A quantum transport simulator based on nonequilibrium Greens' function (NEGF) formalism as described by Datta[16] coupled to a 3D Poisson solver is used. The Poisson equation is solved in 3D coordinates using the method of moments (boundary element method).[17] In the quantum transport model, the device structure is described by a Hamiltonian, H_D, using a simple π-orbital nearest-neighbor tight-binding model.[18] Electron-electron interactions are accounted by the self-consistent potential, ϕ, calculated by the Poisson solver. In the next section we describe these two parts of the simulation process in detail.

Quantum transport simulation: The Hamiltonian of the device is expressed using a π orbital nearest-neighbor tight binding (TB) approximation in the form

$$H_D = \sum_{ij} (t|i\rangle\langle j| - q\phi_D \delta_{ij}), \tag{1}$$

where the first term in the brackets (corresponding to coupling between orbitals) is nonzero only the nearest neighbor atoms and is zero for $i=j$ (on-site interaction).[8] The coupling parameter is taken to be $t=-3$ eV (Ref. 18) which accurately produces the band structure of graphene. The term, ϕ_D, is the self-consistent electrostatic potential calculated by the Poisson solver. The Green's function is then determined by

$$G(E) = [(E + i0^+)I - H_D - \Sigma_S - \Sigma_D]^{-1}, \tag{2}$$

where I is the identity matrix, Σ_S and Σ_D are the self-energies for the left (source) and right (drain) reservoirs. The local density of states resulting from the source/drain injected states is calculated using
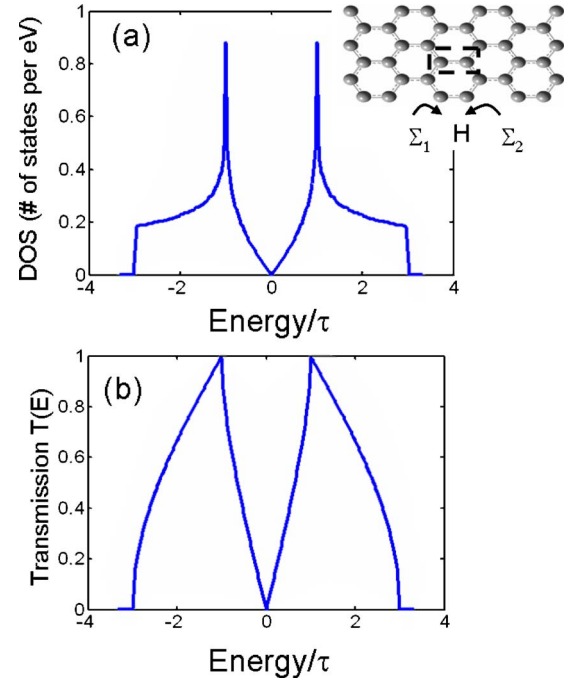

FIG. 1. (Color online) Density of states and transmission of an infinite 2D graphite sheet vs energy/τ, where τ is the π orbital coupling of a tight-binding model. (Obtained by using the recursive surface Green's function approach.) The results are in a good agreement with Ref. 18.

$$DOS_{S(D)}(E) = (1/2\pi)G\Gamma_{S(D)}G^+, \tag{3}$$

where $\Gamma_{S(D)} = i(\Sigma_{S(D)} - \Sigma_{S(D)}^+)$, is the broadening due to the source/drain contacts. The electron correlation function is computed by

$$G^n(E) = G\Sigma^{in}G^+, \tag{4}$$

where, in the ballistic case, the in-scattering function corresponding to the contacts is determined by $\Sigma_{S(D)}^{in}(E) = \Gamma_{S(D)}(E)f(E, E_{FS(D)})$, using the corresponding Fermi distribution function of each reservoir. The charge density is calculated by integrating the electron correlation function $G^n(E)$ in energy as[16,19,20]

$$\rho_j = e \int_{-\infty}^{\infty} \frac{dE}{2\pi} G_j^n(E). \tag{5}$$

After convergence, the current is calculated by[16,19,20]

$$I_{j \to j+1} = \frac{ie}{h} \int_{-\infty}^{-\infty} \frac{dE}{2\pi} [H_{j,j+1}G_{j+1,j}^n(E) - H_{j+1,j}G_{j,j+1}^n(E)]. \tag{6}$$

The self-energies, Σ_S and Σ_D, for the left and right reservoirs are calculated using the Sancho-Rubio iterative method,[21] and describe the effect of infinite length reservoirs.

Using the NEGF approach, the density of states, $DOS(E)$, and transmission, $T(E)$, for an infinite graphene sheet are first calculated. The inset of Fig. 1 shows a schematic of the partition of the device into the channel (an elementary lattice cell consisting of two atoms in this case) and the contacts. The $DOS(E)$ and $T(E)$ are also shown. There is excellent agreement between these results and pre-
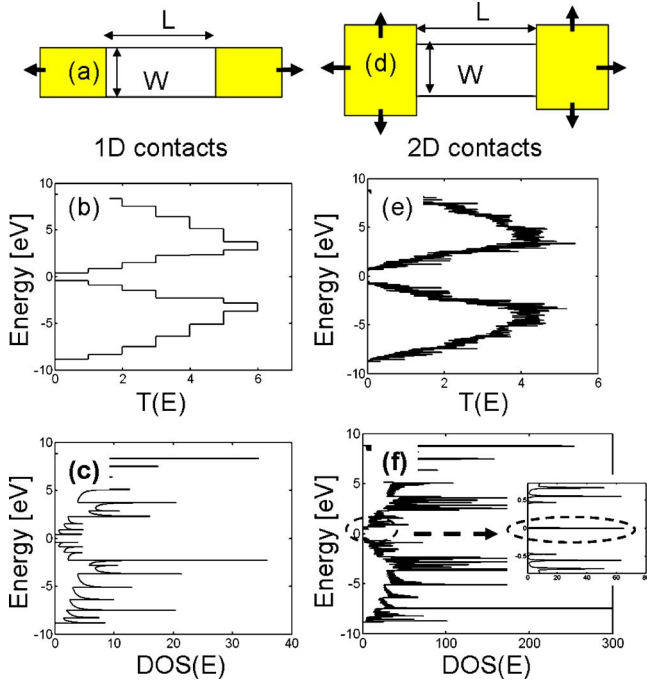
FIG. 2. (Color online) (a) and (d) Schematics of the top view of the device structures for 1D and 2D contacts, respectively. (b), (c) Transmission coefficient and density of states, respectively, vs energy of a 1.4 nm wide GNR with 1D contacts showing the perfect 1D transmission and DOS. (e), (f) Transmission coefficient and density of states, respectively, vs energy of a 1.4 nm GNR with 2D infinite contacts (semi-infinite graphene sheet).

vious studies,[18] which demonstrates that the computed self-energy gives an accurate description of an infinitely extended reservoir. In this work, we implement two types of boundary conditions depending on the nature of the contacts that we want to employ. Specifically, the first type is the 1D contacts, where we assume that the nanoribbon extends to infinity having the same width as in the channel. The second case is the 2D contact case, in which we assume that the contact is a 2D semi-infinite graphene sheet connected to the channel as indicated in the schematics of Fig. 2. There are two signature differences between 1D contact and 2D contact GNR devices. Due to the interface mismatch in the 2D contact case, strong oscillations appear in $T(E)$ and DOS(E). The effect decreases if the channel length (L) is much larger than its width (W). Moreover, in the 2D contact case, a localized state in the middle of the band gap appears due to the metallic contact behavior of the graphene sheet (MIGS). When the channel is long enough, these states are localized at the interface and do not contribute to current. However, they can still cause Fermi level pinning and degrade the device performance.

3D Poisson equation: We employ a 3D electrostatics solution for the device using the method of moments (boundary element method).[17,22] A three-dimensional treatment is necessary in our case because there is no obvious symmetry in the structure that can reduce the treatment of the device to a lower dimensionality with reasonable approximations. The main difference between nanoribbon devices and conventional Si MOSFETs is that in the Si MOSFET the width of the channel alters the transport properties of the MOSFET in a trivial way (i.e., if the width is doubled, the current

doubles). In the case of the ribbons, however, this is not the case since the electronic properties of the ribbon are a sensitive function of its width. The method of moments is a suitable method for treating the electrostatics of these type of devices.

The charge and the potential are separated into the graphene-device (n_D, Φ_D) and the gate/source/drain-boundary (n_B, Φ_B) parts. Grid points are placed only on the regions of the structure on which charge can reside. For the boundary, these are only the surfaces of the source, drain and gate electrodes. Device grid points are placed on all the graphene atoms, on which charge can reside. The elements on the boundary surfaces are assumed to be rectangles with differential element ΔS, and the elements of the device (graphene sheet) are circles with radius R_{eff} (0.2 nm used in this study). The charge distribution is assumed to be composed of point charges in the center of the differential element. The potential at the boundary and device is related to the charge density in the structure by

$$\begin{Bmatrix} \Phi_D \\ \Phi_B \end{Bmatrix} = K(r;r')\begin{Bmatrix} n_D \\ n_B \end{Bmatrix} = \begin{bmatrix} A & B \\ C & D \end{bmatrix}\begin{Bmatrix} n_D \\ n_B \end{Bmatrix}, \quad (7)$$

where K is the electrostatic Kernel of the device geometry under examination. The matrices, A, B describe the contribution of device and boundary charge respectively on the potential on the device, and C, D describe the contribution of device and boundary charge respectively on the potential on the boundary. Under point charge approximation, the potential Φ_i at each element consists of an on-site potential Φ_{ii} and a summation term for the contribution to that potential of all the charges in the system, as follows:

$$\Phi_i = \Phi_{ii} + \sum_{j \neq i}^{N} \frac{\rho_{sj}\Delta S_j}{4\pi\varepsilon |r_i - r_j|}, \quad (8)$$

$$\Phi_{ii} = \frac{Q_{\text{tot}}}{4\pi\varepsilon R_{\text{eff}}} = \frac{\rho_{si}\Delta S_i}{4\pi\varepsilon\sqrt{\Delta S_i/4}} = \frac{\rho_{si}\sqrt{\Delta S_i}}{2\pi\varepsilon}, \quad (9)$$

where Φ_{ii} is the on-site energy of the rectangular surfaces on the boundary nodes. The effect of charge imaging due to the presence of different dielectric regions in the device is also taken into account. Once the electrostatic Kernel $K(r,r')$ is built, the potential on the device can be calculated from (8) to be

$$\Phi_D = (A - BD^{-1}C)n_D + BD^{-1}\Phi_B. \quad (10)$$

The details of this computation are described in Ref. 22.

III. RESULTS AND DISCUSSION

The electronic properties of GNRs along various orientations have been widely studied.[7,8,23,24] Using simple π-orbital tight-binding approaches, zigzag GNRs and armchair GNRs have been predicted to have metallic and semiconducting properties, respectively. Although a recent theoretical study showed that zigzag GNRs can also have a small band gap when spin effects are considered,[25] the band gap is too small to be used for MOSFET-type devices. In this work,

therefore, we focus on exploring the physical properties and device performance of armchair GNR MOSFETs.

A. 1D contacts versus 2D semi-infinite contacts

The nature of the contacts plays an important role in the transport properties of nanostructures. We explore the dimensional effect of the contacts on the properties of the armchair GNR devices shown in Fig. 2 for two types of contacts, the 1D perfectly coupled contacts, and the 2D semi-infinite contacts. As stated earlier, by 1D contacts we mean that the contact is a physical extension of the channel (having the same width), and it extends infinitely in only one dimension, (therefore 1D). By 2D contacts we define the contact as a semi-infinite graphene sheet, connected to the channel that extends infinitely in two dimensions (therefore 2D). Figures 2(a)–2(c) present the device structure, transmission versus energy, $T(E)$, and density of states versus energy, DOS(E), for 12.5 nm long and 1.4 nm wide armchair GNR with 1D contacts. Due to the perfect contacts, the device behaves just like a homogenous structure in equilibrium. The staircase in $T(E)$ and sharp peaks in DOS(E) reflect the infinite 1D material's characteristics. As the GNR becomes wider, the shapes of $T(E)$ and DOS(E) will become closer to that of 2D graphene sheets, cf., Fig. 1, because the quantum confinement effects become weaker and eventually lose their importance in large size device structures.

Figures 2(d)–2(f) show the device structure, transmission versus energy, $T(E)$, and density of states versus energy, DOS(E), respectively, for 60 nm long and 1.4 nm wide armchair GNR with 2D contacts. Compared to the results of the GNR device with 1D contacts, the overall shapes of $T(E)$ and DOS(E) of two cases are similar. The small oscillations on the curves are attributed to reflections from the interfaces between the ribbon and the graphene half-plane. A localized peak appears in the middle of the band gap in Fig. 2(f) resulting from the metallic property of the 2D graphene sheet. Since the Fermi level of the intrinsic GNR also resides at midgap, the metal-induced gap states are expected to cause Fermi level pinning and degrade the device performance. Although these do not affect the transmission [Fig. 2(e)] for long channel devices under equilibrium, they are expected to contribute to tunneling currents in particularly in short channel devices. They can also affect longer channel devices by enhancing scattering processes under high drain bias. In order to examine the performance potential of ballistic GNR MOSFETs, we focus in this article on armchair GNR MOSFETs with 1D perfect contacts.

B. Performance of armchair GNR MOSFETs

To explore the performance of armchair GNR MOSFETs with 1D contacts, a double gate MOSFET structure as shown in Fig. 3 is used. Figure 3(a) shows the side view of the device, where the GNR is placed between two insulator layers, assumed to be SiO$_2$ of 1 nm thickness. Gate electrodes are placed in the top and bottom of the insulators. The source and drain regions are assumed to be doped GNR regions with 0.08 electrons per carbon atom, corresponding to 1.37 $\times 10^8$ electrons/m. Figure 3(b) shows the top view of the
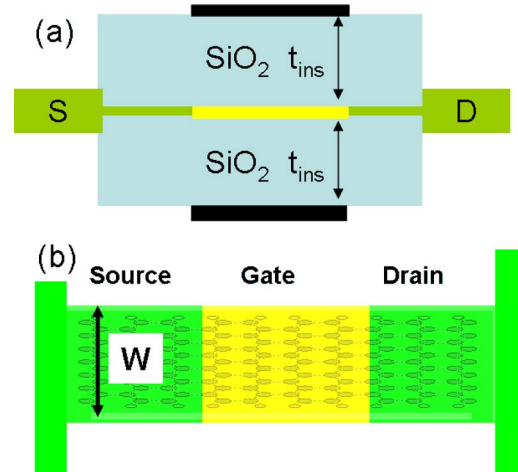

FIG. 3. (Color online) (a) A schematic diagram of the simulated dual-gate carbon nanoribbon MOSFETs. The source and drain are heavily doped nanoribbon contacts while the channel is undoped. The oxide thickness (t_{ins}) is 1 nm in this study. (b) Top view of (a).

GNR channel. (We note here that all parts of the device are treated in 3D. For example, the insulators that surround the GNR are cuboids in 3D with 1 nm thickness. For the calculations in this work, the width of the insulators and the metallic gates are assumed to be twice the GNR width. The length of the gate is equal to the length of the undoped channel and the length of the insulators is equal to the length of the whole simulated device.) In this work, a 1.4 nm wide and a 1.8 nm wide armchair GNR, with a band gap of approximately 0.8 eV and 0.66 eV, respectively, are used to explore the ON-currents and OFF-currents performance of the MOSFET-type device. The channel is assumed to be 12.5 nm long and undoped.

Using the NEGF approach, the local density of states versus energy and position, LDOS(x,E), is calculated. We computed the density of states of the device according to the realistic atomic positions, but plot LDOS(x,E) by averaging the value per atom in a unit cell. Figure 4(a) shows the LDOS(x,E) in the device under equilibrium, including parts of the source and drain. The upper and lower dashed lines correspond to the energies of the edges of the first conduction subband and the first valence subband of the device. In the conduction band region, the oscillation patterns are attributed to quantum mechanical reflections, whereas the second and third subbands are clearly visible. The separations of the subbands are around 0.5 and 0.7 eV which agrees with the subband separations obtained from the dispersion relations in an infinitely long 1.4 nm wide armchair GNR. The strong oscillation patterns of the LDOS visible in the source and drain are also observed in previous theoretical studies of a semiconductor nano-MOSFETs and CNT MOSFETs,[15,26,27] and are created from quantum reflections off the barrier of the channel. The light-gray colored area in the band gap under the first conduction band, especially inside the channel region, corresponds to the density of states caused by the evanescent tail of the electron wave function inside the source and drain that penetrates into the undoped channel region. Under certain operating bias, these states could contribute to tunneling and degrade the device performance. In
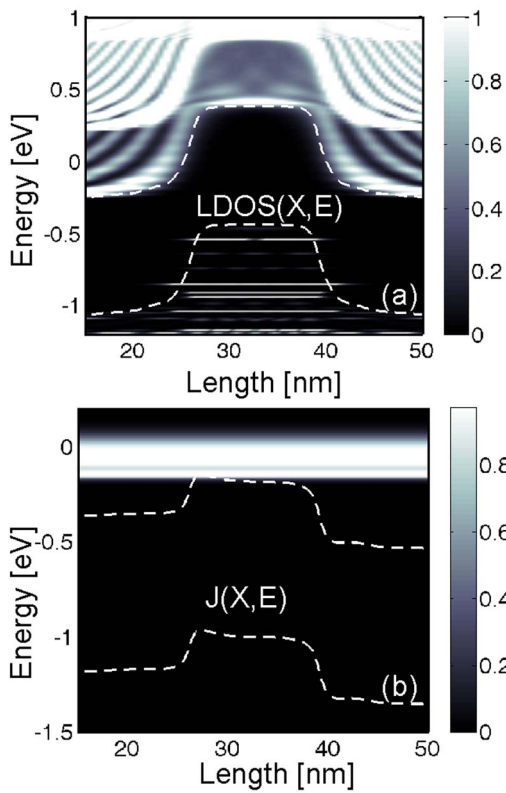
FIG. 4. (a) The local density of states, LDOS(x,E), at equilibrium. Dashed lines show the band profile of the lowest conduction band and the highest valence band of 1.4 nm width armchair GNR. The second and third conduction subbands are clearly seen in the plot, as well as quantum levels in the valence band due to longitudinal confinement. (b) The ballistic current density spectrum, $J(x,E)$, normalized by q^2/h, for $V_G=0.7$ V and $V_D=0.4$ V. Current contribution comes from electrons above the top of the barrier and below the Fermi level of the source ($E_{FS}=0$ in this case).

FIG. 5. (Color online) (a) Simulated current I_{DS} vs V_{DS} for a 1.4 nm wide and 12.5 nm channel long armchair GNR at $V_{GS}=0.3$, 0.4, 0.5, and 0.6 V. (b) Simulated current I_{DS} vs V_{GS} for a 1.4 nm wide and 12.5 nm long channel armchair GNR at $V_{DS}=0.05$ and 0.4 V, as well as for a 1.8 nm wide and 12.5 nm long armchair GNR at $V_{DS}=0.4$ V.

the valence band region, localized states due to quantum confinement effects caused by the quantum well that is formed, can be clearly observed. These states would also contribute to tunneling currents when the top of the valence band is close to the bottom of the conduction band of the source, for example under strong negative gate biases, and hence play an important role to band-to-band tunneling devices. They could be washed out by increasing the channel length or the GNR width.

Next, we plot the current density spectrum in the transport direction of the channel versus energy, $J(x,E)$. Similarly to LDOS(x,E), the averaged $J(x,E)$ in a unit cell under $V_{DS}=0.4$ V and $V_{GS}=0.7$ V, normalized by q^2/h, is shown in Fig. 4(b). Due to the ballistic transport assumption, the current density is constant at each energy throughout the entire length of the device. The main contribution to the current comes from the energy window region between the chemical potential of the source (located at $E=0$) and the top of the barrier between the source and channel. Quantum simulations capture both thermionic emitted and tunneling currents which can be important. Tunneling currents will be discussed in more detail later on.

The source-to-drain current versus V_{DS} for different V_{GS} values of the armchair GNR MOSFET is shown in Fig. 5(a), indicating good MOSFET-type device behavior. The current
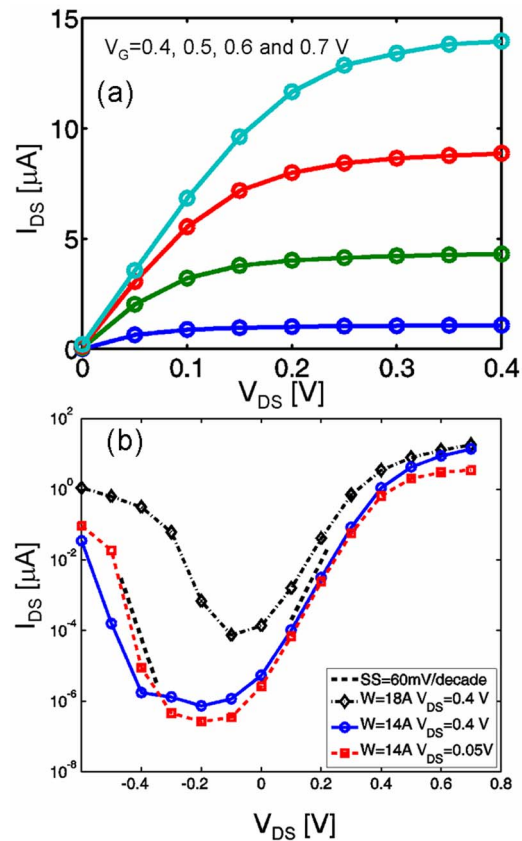
density of these GNR MOSFETs at $V_{GS}=0.6$ V is around 6000 μA/μm, which satisfies the requirement of the 2006 ITRS report for the year 2015.[28] Note that our simulations use thicker insulators and smaller power supply (0.4 V) compared to the projections of the 2006 ITRS report, and no external series resistance was included in our calculations. Figure 5(b) shows the I_{DS}-V_{GS} characteristics of a 1.4 nm and 1.8 nm wide armchair GNR MOSFETs. The corresponding band gaps of the two devices are $E_G=0.8$ eV and $E_G=0.66$ eV, respectively. The DIBL is 30 mV/V and 53 mV/V respectively, whereas the subthreshold swings are 65 mV/dec and 70 mV/dec. These values are smaller than DIBL $=122$ mV/V and $S=90$ mV/decade, that are the estimated values of a double gate, 10 nm scaled Si MOSFETs.[14] This can be attributed to the better gate control on the electrostatics of the GNR MOSFET device compared to Si MOSFETs. A GNR is a monolayer material, i.e., the ultimate ultra-thin body channel. Two-dimensional electrostatic effects, therefore, are suppressed and DIBL is reduced. The fundamental thermal limit of SS$=60$ mV/decade at room temperature is, however, not achieved because the light effective mass of carriers in the GNR and the short channel length in combination with the small band gap enhance source-to-drain tunneling. Due to the smaller band gap, the OFF-state current of the 1.8 nm wide MOSFET is about two orders of magnitude higher than that of the 1.4 nm wide MOSFET, and its SS is
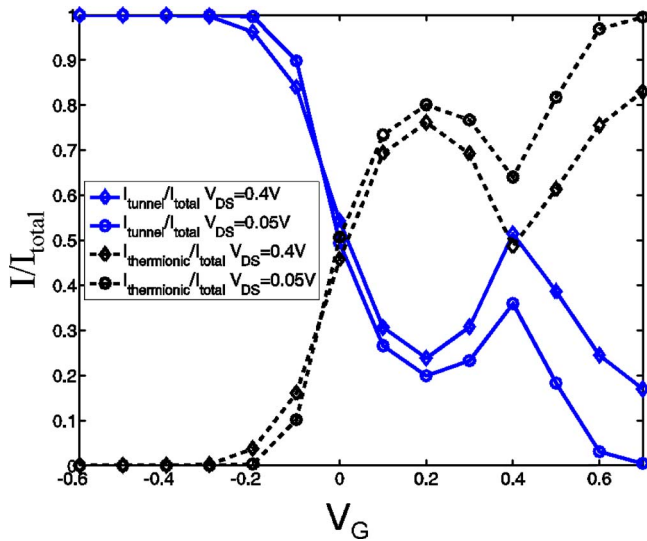
FIG. 6. (Color online) Ratio of the tunneling current (solid line) and thermionic current (dashed line) to the total current at $V_{DS}=0.05$ V (circle) and $V_{DS}=0.4$ V (diamond) for V_{GS} from −0.6 V to 0.7 V. The quantum tunneling current plays an important role in the OFF current when the gate voltage decreases. When V_{GS} is smaller than −0.3 V, the tunneling current dominates the OFF current.
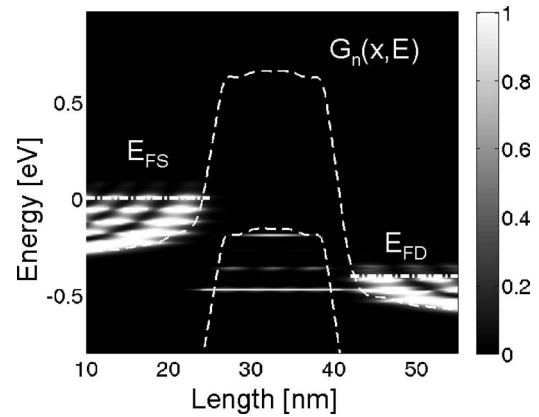

FIG. 7. Simulated $G_n(x,E)$ at $V_{DS}=0.4$ V and $V_{GS}=-0.6$ V. When the quantum levels in the channel's valence band are close to the bottom of source's conduction band, more electrons start tunneling between bands and current starts to increase.

higher too. This quantum tunneling current plays a significantly important role in the OFF-state of MOSFET and SS degradation.

Figure 6 shows the ratio of quantum tunneling current (solid line) and thermionic (dashed line) current to the total current versus V_{GS} bias. The tunneling current is calculated from current contribution under the top of the barrier, and the thermionic current is calculated from the current contribution above the top of the barrier. Both results are presented at $V_{DS}=0.4$ V (diamonds) and $V_{DS}=0.05$ V (circles) for V_{GS} from −0.6 V to 0.7 V. We found that, when V_{GS} decreases (more negative bias), the ratio of quantum tunneling current to the total current increases. This is because the barrier height increases as V_{GS} decreases, reducing all thermally emitted contribution. When V_{GS} is less than −0.2 V, the tunneling current due to band-to-band tunneling mechanisms completely dominates, and thus determines the OFF-current. As V_{GS} increases (more positive bias), the tunneling current decreases (since the band to band tunneling mechanisms are inhibited), but around 0.3 V it increases again due to the quantum tunneling currents under the top of the barrier. Thus the tunneling current plays a less important role when the device is in the ON-state (under high gate bias) because most of electrons would go above the top of the barrier, just like in a classical MOSFET. The tunneling current, however, still cannot be ignored because it contributes about 20% of the total current even at ON-state conditions ($V_G=0.7$ V and $V_{DS}=0.4$ V).

Figure 7 shows the electron density versus energy along the length of the device, $G^n(x,E)$ at $V_D=0.4$ V and $V_G=-0.6$ V. The quantum states in the valence band provide the paths to achieve band-to-band (BTBT) currents. Once these valence band states rise entirely above the bottom of the conduction band of the source (stronger negative gate bias), the current will increase dramatically. This phenomenon ac-

counts for the rise in current at negative bias, see e.g., below $V_G=-0.2$ V in Fig. 5(b). This behavior is similar to that observed experimentally[14] and theoretically[15] for carbon nanotube transistors. BTBT MOSFET operation can be achieved in this way. Since the thermionic-tunneling current can be ignored in these operating conditions, the SS would not follow the thermal limit. Therefore, BTBT MOSFETs are expected to outperform the normal MOSFETs in terms of SS behavior (sub-60 mV/dec at room temperature), something experimentally demonstrated for CNT MOSFETs. (In our simulations there is an indication of this sub-60 mV/dec behavior which can be further enhanced, but an analysis and optimization of a band-to-band tunneling type of device[28] is beyond the scope of this article). Due to the similar electronic structure of GNRs and CNTs, GNRs should also have the potential for BTBT type of MOSFETs applications. This type of device however, might suffer from the low drive current capabilities due to the reduced magnitude of the tunneling currents.[28]

IV. CONCLUSION

In this work, we described the real space quantum transport simulation for GNR FETs using NEGF approach based on a π-orbital TB method. The model was used to investigate the interface properties of an armchair GNR MOSFET with 1D and 2D contacts. Semimetallic 2D graphene sheet contacts induce localized states in the middle of the band gap. These states cause Fermi level pinning and degrade the device performance. We focused, therefore, on the 1D contact case for which no MIGS states occur, and investigated the device performance of a ballistic armchair 12.5 nm channel length GNR MOSFETs with 1.4 nm and 1.8 nm widths. The device structure assumed was a double gate MOSFET with a 1 nm insulator thickness. We found that these GNR MOSFETs have the potential for better performance than a double gate, 10-nm-scale Si MOSFETs in terms of SS, DIBL, and on-current. Although tunneling processes cannot be ignored and degrade the performance of GNR MOSFET-type device, they might find potential applications to GNR MOSFETs operating in the BTBT mode.

ACKNOWLEDGMENTS

[1] A. Javey, J. Guo, Q. Wang, M. Lundstrom, and H. Dai, Nature **424**, 654 (2003).

[2] J. A. Misewich, R. Martel, Ph. Avouris, J. C. Tsang, S. Heinze, and J. Tersoff, Science **300**, 783 (2003).

[3] J. Chen, V. Perebeinos, M. Freitag, J. Tsang, Q. Fu, J. Liu, and P. Avouris, Science **310**, 1171 (2005).

[4] J. Kong, N. Franklin, C. Chou, S. Pan, K. Cho, and H. Dai, Science **287**, 622 (2000).

[5] C. Berger, Z. Song, X. Li, X. Wu, N. Brown, C. Naud, D. Mayou, T. Li, J. Hass, A. N. Marchenkov, E. H. Conrad, P. N. First, and W. A. de Heer, Science **312**, 1191 (2006).

[6] Y. Zhang, J. P. Small, W. V. Ponyius, and P. Kim, Appl. Phys. Lett. **86**, 073104 (2005).

[7] M. Fujita, K. Wakabayashi, K. Nakada, and K. Kusakabe, J. Phys. Soc. Jpn. **65**, 1920 (1996).

[8] G.-C. Liang, N. Neophytos, D. Nikonov, and M. Lundstrom, IEEE Trans. Electron Devices **54**, 677 (2007).

[9] M. C. Lemme, T. J. Echtermeyer, M. Baus, and H. Kurz, IEEE Electron Device Lett. **28**, 282 (2007); Z. Chen, Y. Lin, M. Rooks, and P. Avouris, e-print arXiv:cond-mat/0701599.

[10] B. Obradovic, R. Kotlyar, F. Heinz, P. Matagne, T. Rakshit, D. Nikonov, M. D. Giles, and M. A. Stettler, Appl. Phys. Lett. **88**, 142102 (2006).

[11] G.-C. Liang, N. Neophytou, D. Nikonov, and M. Lundstrom, *Theoretical Study of Graphene Nanoribbon Field-Effect Transistors*, Proceeding of Conference, Nanotech 2007, May 2007.

[12] During the preparation of this article, we become aware of the similar conclusion from G. Fiori and G. Iannaccone, e-print arXiv:cond-mat/arXiv:0704.1875v1.

[13] S. Hasan, J. Wang, and M. Lundstrom, Solid-State Electron. **48**, 867 (2004).

[14] J. Appenzeller, Y.-M. Lin, J. Knoch, and Ph. Avouris, Phys. Rev. Lett. **93**, 196805 (2004).

[15] S. Koswatta, M. Lundstrom, M. P. Anastram, and D. Nikonov, Appl. Phys. Lett. **87**, 253107 (2005).

[16] S. Datta, *Quantum Transport: Atom to Transistor*, 2nd ed. (Cambridge University Press, Cambridge, MA, 2005).

[17] S. Ramo, J. Whinnery, and T. Van Duzer, *Fields and Waves in Communication in Electronics*, 3rd ed. (John Wiley & Sons, Inc., New York, 1993).

[18] R. Saito, G. Dresselhaus, and M. Dresselhaus, *Physical Properties of Carbon Nanotubes* (Imperial College Press, London, 1998).

[19] R. Lake, G. Klimeck, R. Bowen, and D. Jovanovic, J. Appl. Phys. **81**, 7845 (1997).

[20] S. Koswatta, S. Hasan, M. Lundstrom, M. P. Anantram, and D. Nikonov, e-print arXiv:cond-mat/0702496.

[21] M. P. L. Sancho, J. M. L. Rubio, and J. Rubio, J. Phys. F: Met. Phys. **15**, 851 (1985).

[22] N. Neophytou, M. Lundstrom, and J. Guo, J. Comput. Electron. **3**, 277 (2004).

[23] M. Ezawa, Phys. Rev. B **73**, 045432 (2006).

[24] Y. W. Son, M. L. Cohen, and S. G. Louie, Phys. Rev. Lett. **97**, 216803 (2006).

[25] Y. W. Son, M. L. Cohen, and S. G. Louie, Nature **444**, 347 (2006).

[26] R. Venugopal, Z. Ren, S. Datta, M. S. Lundstrom, and D. Jovanovic, J. Appl. Phys. **92**, 3730 (2002).

[27] J. Wang, E. Polizzi, and M. Lundstrom, J. Appl. Phys. **96**, 2192 (2004).

[28] S. Koswatta, D. Nikonov, and M. Lundstrom, Tech. Dig. - Int. Electron Devices Meet. **1**, 518 (2006).
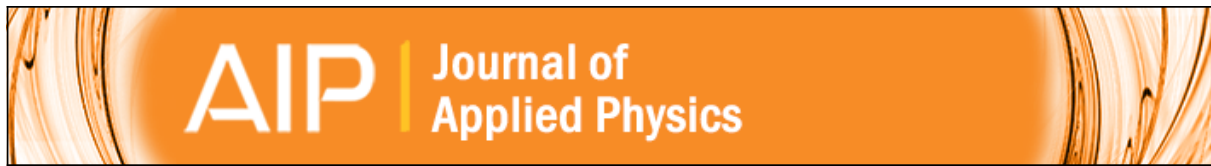
Gengchiau Liang, Neophytos Neophytou, Mark S. Lundstrom, and Dmitri E. Nikonov

---

Articles you may be interested in

Modeling of quasi-ballistic transport in nanowire metal-oxide-semiconductor field-effect transistors
J. Appl. Phys. **118**, 155105 (2015); 10.1063/1.4933287

Effect of intravalley acoustic phonon scattering on quantum transport in multigate silicon nanowire metal-oxide-semiconductor field-effect transistors
J. Appl. Phys. **108**, 034510 (2010); 10.1063/1.3457848

Experimental evidence of ballistic transport in cylindrical gate-all-around twin silicon nanowire metal-oxide-semiconductor field-effect transistors
Appl. Phys. Lett. **92**, 052102 (2008); 10.1063/1.2840187

Ballistic quantum transport in a nanoscale metal-oxide-semiconductor field effect transistor
Appl. Phys. Lett. **91**, 103510 (2007); 10.1063/1.2780058

Quantum transport in a nanosize double-gate metal-oxide-semiconductor field-effect transistor
J. Appl. Phys. **96**, 2305 (2004); 10.1063/1.1767619